Accepted Article

Title: Efficient Broadband Near-Infrared Emission from Lead-Free Halide Double Perovskite Single Crystal

Authors: Gangyi Zhang, Deyin Wang, Bibo Lou, Chong-Geng Ma, Andries Meijerink, and YuHua Wang

WILEY-VCH

WILEY-VCH

Efficient Broadband Near-Infrared Emission from Lead-Free Halide Double Perovskite Single Crystal

Gangyi Zhang[a], Deyin Wang[a], Bibo Lou[b], Chong-Geng Ma[b], Andries Meijerink[a,c],*, Yuhua Wang[a],*

G. Zhang, D. Wang, B. Lou, Prof. C.-G. Ma, Prof. A. Meijerink, Prof. Y. Wang

[a] School of Materials and Energy, National and Local Joint Engineering Laboratory for Optical Conversion Materials, Lanzhou University, Lanzhou, 730000, China.

[b] School of Optoelectronic Engineering & CQUPT-BUL Innovation Institute, Chongqing University of Posts and Telecommunications, Chongqing, 400065, China.

[c] Condensed Matter and Interfaces, Debye Institute for Nanomaterials Science, Utrecht University, 3508 TA Utrecht, The Netherlands.

E-mail: *wyh@lzu.edu.cn, A.Meijerink@uu.nl.*

Ultra-broadband near-infrared (NIR) luminescent materials are the most important component of NIR light-emitting devices (LED) and are crucial for their performance in food detection, medical and bio-sensing applications. A major challenge at this stage is to design novel NIR luminescent materials to replace the traditional Cr^{3+}-doped systems. This work reports an all-inorganic bismuth halide perovskite $Cs_2AgBiCl_6$ single crystal that achieves efficient broadband NIR emission by introducing Na ions. Experiments and density functional theory (DFT) calculations show that the NIR emission originates from self-trapped excitons (STE) emission, which can be enhanced by weakening the strong coupling between electrons and phonons. The high photoluminescence quantum efficiency (PLQY) of 51%, the extensive full width at half maximum (FWHM) of 270 nm and the outstanding stability provide important advantages of $Cs_2Ag_{0.05}Na_{0.95}BiCl_6$ single crystal as a NIR luminescent material. The single crystal based NIR LED demonstrated its potential applications in NIR spectral detection as well as night vision. This work demonstrates that the bismuth halide perovskites are promising

1

WILEY-VCH

candidates for broadband NIR luminescent materials and provides new application directions for luminescent metal halides.

Introduction

NIR light sources have a widespread application in the fields of food quality testing and analysis, medical diagnosis, health monitoring and night vision due to their large penetration depth, low thermal effect and non-toxicity.[1] In particular, the NIR light sources in the range of 700-1100 nm have received more attention because the tissues of various components in food and human body have characteristic absorption in this region. In addition, this wavelength range matches well with inexpensive and sensitive silicon-based photodetectors to build a compact spectral analysis system, which is suitable for rapid detection in daily life.[2] To realize these applications, small, portable and efficient broadband emitting NIR light sources are necessary. However, traditional NIR light sources such as tungsten halogen lamps with continuous broadband emission are still limited by their large size, low efficiency and short lifetime.[3] Therefore, in order to obtain high-performance NIR LEDs, efficient broadband NIR light-emitting materials under near-ultraviolet or blue-light chip excitation are widely investigated.

In early studies, rare earth ions Pr^{3+}, Nd^{3+}, Tm^{3+} and Sm^{3+} were used as activators to obtain the NIR luminescence.[4] However, their performance is unsatisfactory due to the limited emission range, sharp spectral features and light absorption caused by the parity-forbidden intraconfigurational 4f-4f transitions. Eu^{2+} ions with 4f-5d transitions typically exhibit broad emission in the ultraviolet or visible spectral region, but in some specific systems, it can also show broadband NIR emission but until now no NIR Eu^{2+} phosphor with emission extending to 1000 nm has been found.[5] A promising activator ion is Cr^{3+}. Due to the wide excitation range, unique energy level structure and controllable broadband emission in weak crystal field coordination ($^4T_2 \rightarrow {}^4A_2$ transition), Cr^{3+} ions are often used as activators for NIR luminescent materials.[6] Furthermore, phosphors doped with Cr^{3+} have been widely reported due to their high quantum efficiency and thermal stability, such as $Na_3Al_2Li_3F_{12}:Cr^{3+}$, $Ca_3Sc_2Si_3O_{12}:Cr^{3+}$,

2

WILEY-VCH

LiGaP$_2$O$_7$:Cr^{3+}.[7] However, the emission of these Cr^{3+} doped phosphors are not broad enough to fully cover the first NIR window (NIR-I, 650-950 nm),[8] and the FWHM can only reach around 200 nm even after optimization by co-doping Yb^{3+}.[9] In addition, the preparation of phosphor containing Cr^{3+} can be accompanied by the production of Cr^{6+}, which is a substance with potential carcinogenic risk.[10] Therefore, it is urgent to explore new materials systems with broadband NIR emission.

Metal halide perovskites and their derivatives have attracted more and more attention due to their excellent optoelectronic properties and are considered as a new generation of light-emitting materials.[11] Through the substitution of alkali metal and halogen elements, the emission of metal halide perovskites can be tuned in the entire visible light range to achieve high efficiency emission and even the white emitting from a single host.[12] Since the first discovery of wavelength tunable NIR emission in tin halide perovskites, a great number of NIR emitting metal halide materials have been discovered.[13] Among them, the ns^2 electron configuration ions Sn^{2+}, Sb^{3+}, Bi^{3+} are widely used as activators to get broadband emission by self-trapped excitons (STEs).[14],[15],[16] Recently, Chen's group designed and synthesized a Sn^{2+} doped 2D lead halide perovskite PEA$_2$PbI$_4$, showing a broadband NIR emission peaking at 700 nm. Although the PEA$_2$PbI$_4$:Sn^{2+} has a PLQY up to 42%, its practical applications are restricted by the highly toxic Pb^{2+} ions and the stability is compromised by the easily oxidized Sn^{2+}.[14a] More recently, Sb^{3+} doped metal halides have been extensively investigated on account of their oxidation resistance, low toxicity and high chemical activity. Substitution of Cs$^+$ ions by Rb$^+$ ions in Sb^{3+} doped all-inorganic lead-free 0D In-based perovskites was shown to cause the broadband NIR emission shift from 700 nm to 750 nm. These materials are also difficult to use in practice in that the PLQY drops from 36% to 21% as the emission spectrum red shifts.[17] Xia's group reported a Sb^{3+} doped zinc halide single crystal which has a broad NIR emission peaking at 745 nm with a high PLQY of 70% and a FWHM of 175 nm.[18] Single crystals can greatly reduce light losses due to the surface defects and achieve efficient emission, but the

3

WILEY-VCH

excitation spectrum of the sample does not match with the commonly used near-ultraviolet chips and the FWHM of the emission is not sufficient, which will limit its practical applications.

In this work, we report an all-inorganic bismuth halide $Cs_2AgBiCl_6$ single crystal with a double perovskite structure. We found the non-radiative relaxation by strong electron-phonon coupling to be the main reason for the poor emission efficiency of $Cs_2AgBiCl_6$ single crystal at room temperature. The introduction of Na ions brings excellent luminescence properties, and under the excitation at 365 nm, $Cs_2Ag_{0.05}Na_{0.95}BiCl_6$ single crystal emits efficient broadband NIR emission peaking at 700 nm with PLQY of 51%, FWHM of 270 nm, and large Stokes shifts of 340 nm at room temperature. The enhanced luminescence is mainly caused by localization of electrons and holes and reducing non-radiative decay processes due to electron-phonon coupling for trapped excitons and an increase in the binding energy of excitons. In addition, we demonstrate the excellent stability of $Cs_2Ag_{0.05}Na_{0.95}BiCl_6$ single crystal, which maintains structural integrity at 550 ℃ and the room temperature quantum efficiency is still above 90% of the initial value after long-term storage in humid air. Benefiting from the various properties of $Cs_2Ag_{0.05}Na_{0.95}BiCl_6$ single crystal, a NIR LED was fabricated to demonstrate their potential applications in NIR spectroscopy and night vision. This work demonstrates the feasibility of achieving efficient broadband NIR emission in Bi-based metal halides and provides new insights into the NIR emission of metal halide systems.

Results and Discussions

Single crystals of $Cs_2AgBiCl_6$ and $Cs_2Ag_{1-x}Na_xBiCl_6$ were synthesized via a solvothermal method. The actual composition of the $Cs_2Ag_{1-x}Na_xBiCl_6$ was determined by inductively coupled plasma optical emission spectrometry (ICP-OES), and the corresponding results were shown in Table S1 (Supporting information). $Cs_2AgBiCl_6$ crystalizes into double perovskite 3D structure, in which each Bi and Ag atom are coordinated with six Cl^- ions to form $[BiCl_6]^{3-}$ and $[AgCl_6]^{5-}$ units, and $[BiCl_6]^{3-}$ and $[AgCl_6]^{5-}$ octahedrons alternatively stack with Cs atoms

4

occupying the gaps in the 3D structure (Figure 1a). $Cs_2AgBiCl_6$ has a cubic Fm-3m space group with cell parameters of a=b=c=10.7755(6) Å, α=β=γ=90∘ as was determined by single-crystal X-ray diffraction (SCXRD) measurement. $Cs_2NaBiCl_6$ has the same crystal structure as that of $Cs_2AgBiCl_6$, and its cell parameters were determined to be a=b=c=10.8375(6) Å (Table S2 Supporting Information). The ionic radius of Na^+ is slight larger than that of Ag^+ and the lattice constant mismatch between these two crystals is as small as 0.57%, which demotes that they may form highly miscible $Cs_2(Ag,Na)BiCl_6$ alloys. The high phase purity of the resultant $Cs_2Ag_{1-x}Na_xBiCl_6$ crystal was confirmed by the coincidence of measured powder X-ray diffraction (PXRD) pattern with calculated single crystal data (Figure 1b). The PXRD patterns of as-prepared $Cs_2Ag_{1-x}Na_xBiCl_6$ with nominal Na contents of 0, 25%, 50%, 75%, 95% and 100%, agree well with the calculated SCXRD data. With the increasing of the Na content in $Cs_2Ag_{1-x}Na_xBiCl_6$, the (220) diffraction peak shifted toward lower 2θ angles accompanied by the obvious intensity increase of the (111) diffraction peak, whose intensity is dependent on the increase of Na/Ag composition through the lattice dispersion factor of the Na, Ag and Bi atoms (Figure S1 Supporting Information).[19] Furthermore, compared with the $Cs_2AgBiCl_6$, $Cs_2Ag_{0.05}Na_{0.95}BiCl_6$ exhibited a slight enlarged interplanar distance (from 0.380 nm to 0.383 nm) (Figure 1c). The increased interplanar distance and the homogeneous element distribution (Figure 1d) verify the successful doping of Na ions and confirm the formation of the alloyed structure. Moreover, the XPS analysis confirmed all the elements in the samples are in the expected oxidation states. The typical binding energy corresponds to the Cs 3d, Ag 3d, Bi 4f, Na 1s and Cl 2p, after calibration of the energy scale on the C 1s peak at 284.8 eV. Compared to $Cs_2AgBiCl_6$, the binding energies of Cs, Bi and Cl are slightly increased while that of Ag is decreased, signifying that the introduction of Na substitution at the Ag site causes the formation of $[NaCl_6]^{5-}$ octahedron instead of $[AgCl_6]^{5-}$ octahedron (Figure S2 Supporting Information).

The single crystal $Cs_2AgBiCl_6$ is light yellow and transparent, and becomes colorless with the increase of Na content, which due to a blue shift of the absorption edge. Both the

5

WILEY-VCH

$Cs_2AgBiCl_6$ and $Cs_2NaBiCl_6$ have similar absorption characteristics, with an onset around 490 nm and 420 nm, respectively. Moreover, the absorption spectra of series samples $Cs_2Ag_{1-x}Na_xBiCl_6$ gradually shift to shorter wavelength region as the Na ions content increases (Figure 2a). The PL spectra, PLQY measurement and PLE spectra of the full series were recorded at room temperature. For the $Cs_2Ag_{1-x}Na_xBiCl_6$ single crystals, broad emissions cover the 500 nm to 1100 nm range peaking at about 700 nm can be observed under the excitation of 365 nm (Figure 2b). With increasing of the Na ions content, the PL intensity, PLQY increase while the emission decay times lengthen. However, When the Na ions completely replace Ag ions to form $Cs_2NaBiCl_6$, the luminescence properties are changed due to the transition to an entirely different system.[20] For the optimum Na content, $Cs_2Ag_{0.05}Na_{0.95}BiCl_6$ shows a broad emission band with a FWHM of 270 nm and a large Stokes shift of 340 nm and a long lifetime of 3.05 μs at room temperature (Figure 2b, c). At low temperature, the decay time of series samples has the same trend as that at room temperature (Figure S3 Supporting Information). Importantly, the PLQY of the $Cs_2Ag_{0.05}Na_{0.95}BiCl_6$ single crystal is up to 39%, which was determined for a wavelength range that does not cover the entire emission spectrum. After using Gaussian function to fit and complete the spectrum, the PLQY can reach to 51%, which is better than the reported value for Bi-based bulk perovskite (Figure S4 Supporting Information). This high PLQY shows that the $Cs_2Ag_{0.05}Na_{0.95}BiCl_6$ single crystal can effectively suppress thermal quenching and non-radiative transitions. In order to probe the origin of the broad red emission, the PLE spectra moniotring the emissions from 550 nm to 820 nm were characterized. The PLE spectra show almost the same shapes and characteristics, indicating that the broad emission comes from the same excited state (Figure 2d). We also measured the PL spectra under different excitations, and we can find the emission peak of the sample has a slight red shift when using lower energy to excite the sample (Figure S5 Supporting Information).[15e] To investigate the origin of the emission, power dependent measurements were carried out. The linear relationship between the excitation power and the PL intensity (over 1.7 W/cm^2) rules

out that the origin of the emission is caused by permanent defects (Figure 2e, Figure S6 Supporting Information).[21] Furthermore, the time-resolved PL spectra from 6 μs to 22 μs measured at different wavelengths from 500 nm to 1000 nm (Figure 2f) and the time-resolved photoluminescence (TRPL) mapping also support the presence of a single type of radiative recombination process that is intrinsic to the host lattice (Figure S7 Supporting Information). Finally, in view of the the broadband emission, the large Stokes shift and long PL decay time, the oberved broad emission is attributed to the STEs. The STE emission is independent on the band edge states, so the incorporation of Na only changes the band gap of $Cs_2NaBiCl_6$ but has little effect on the PL peak position.[22]

In order to better understand the origin of the NIR emission, the PBE-DFT calculations with taking into account the spin-orbit coupling (SOC) effect were firstly performed to acquire the knowledge of the electronic structures of $Cs_2(Ag,Na)BiCl_6$ bulks. The calculated compound $Cs_2AgBiCl_6$ shows an indirect bandgap of 1.57 eV starting from the *X* point and ending at the *L* point, and its valence band maximum (VBM) is mainly derived from the Ag-4d and Cl-3p orbitals, whereas the corresponding conduction band minimum (CBM) is primary composed of the Bi-6p and Cl-3p orbitals (Figure 3a, Figure S8a Supporting Information). As for $Cs_2NaBiCl_6$, a larger indirect bandgap of 3.01 eV is exhibited from the VB's *X* point to the CB's *G* point, as shown in Figure S8b (Supporting Information). The Inspection of Figure 3b reveals that the components of CBM are similar with those in $Cs_2AgBiCl_6$, but the VBM of $Cs_2NaBiCl_6$ is composed of the Bi-6s and Cl-3p orbitals. The calculated mixed case $Cs_2Ag_{0.06}Na_{0.94}BiCl_6$ given in Figure 3c indicates that the increase in the band gap after alloying with Na ions is consistent with the result extracted from the experimental absorption spectra, although the orbital components of Na ions hardly contribute to the band edges. The hybrid HSE06 calculations with the SOC consideration were used to further improve the description of the electronic structures of all the calculated compounds. It can be found that the fundamental band gap of neat $Cs_2NaBiCl_6$ is increased to 3.92 eV and the slightly doping of Ag ions can introduce

7

the Ag-4d orbital components into the VBM. In conclusion, the increase of Na contents replacing Ag ones can result in widening the narrow band gap of $Cs_2AgBiCl_6$ caused by the strong coupling between Ag^+ and Cl^- ions.[23]

More charge-density and geometry optimization calculations were implemented to understand the role of doping Na ions for the bright NIR emission and to reveal the lattice distortions in atomic scale, respectively. For $Cs_2AgBiCl_6$, the electrons remain strongly confined in a single $[BiCl_6]^{3-}$ octahedron, whereas the holes are distributed in the surrounding Ag ions (Figure 4a). The lattice distortion happens between the adjacent $[AgCl_6]^{5-}$ and $[BiCl_6]^{3-}$ octahedrons when the STE state is formed, as shown in Figure 4b and 4c. For Na-rich compounds, such as $Cs_2Ag_{0.06}Na_{0.94}BiCl_6$, the introduced $[NaCl_6]^{5-}$ octahedrons will separate the $[AgCl_6]^{5-}$ octahedrons and further reduce the electronic dimensionality of the $Cs_2AgBiCl_6$ lattice.[24] More importantly, the newly-formed $[NaCl_6]^{5-}$ octahedrons act as the barriers to confine the spatial distribution of the STE state, and therefore both holes and electrons have to be localized around the adjacent $[AgCl_6]^{5-}$ and $[BiCl_6]^{3-}$ octahedrons. This indeed enhances the overlap between the electron and hole orbitals and further leads to the easier formation of the trapped excitons.[25] Such fact is confirmed by the calculated charge-density contours of the STE state in $Cs_2Ag_{0.06}Na_{0.94}BiCl_6$ given in Figure 4d. The lattice distortion of the STE state was also calculated and shown in Figure 4e and 4f. Although the very similar results on the excited state structure and the emission band profile can be easily seen as those of $Cs_2AgBiCl_6$, the electron-phonon coupling effect is weakened due to the isolation of the $[AgCl_6]^{5-}$ octahedrons by Na^+ doping.

In order to gain more insight into the photophysical mechanisms of $Cs_2AgBiCl_6$ and $Cs_2Ag_{0.05}Na_{0.95}BiCl_6$, the temperature-dependent PL were further investigated. It has been pointed out above that the emission of $Cs_2AgBiCl_6$ is barely visible at room temperature. When the temperature is decreased to 150 K, an emission band with a maximum around 630 nm can be observed. The PL intensity continued to increase as the temperature was further decreased

8

to 4 K, indicating that nonradiative recombination is suppressed at low temperature. Upon cooling temperature, the emission of $Cs_2Ag_{0.05}Na_{0.95}BiCl_6$ shows same trend (Figure 5a, b, Figure S9 Supporting Information). According to the temperature-dependent PL intensity, the exciton binding energy (E_b) of the two samples can be calculated by fitting the equation[27]:

$$I(T) = \frac{I_0}{1+A\cdot\exp(-E_b/k_BT)}$$

(1)

Where I_0 is the integrated PL intensity at 0 K, and k_B is the Boltzmann constant. For $Cs_2AgBiCl_6$, a low exciton binding energy 16.7 meV can be obtained, which imply that may be not suitable for lighting applications. In contrast, for $Cs_2Ag_{0.05}Na_{0.95}BiCl_6$, we obtain a much higher exciton binding energy of 139.8 meV (Figure 5c), which can ensure the survival of excitons and enable the efficient emission (PLQY≈51%) at room temperature. In addition, the red shift of the emission peak and the narrowing of the spectrum during the decrease of temperature were observed in both samples. The energy of STEs emission (E_{PL}) can be described by the following equation[22]:

$$E_{PL} = E_g - E_b - E_{st} - E_d \tag{2}$$

Where the energy gap, the exciton binding energy, the self-trapping energy and the lattice deformation energy were abbreviated as E_g, E_b, E_{st} and E_d, respectively. Similar to the previous report $CsPbBr_3$, $Cs_3Bi_2Br_9$ and $Cs_3Sb_2Br_9$, the lattice deformation is the reason why the STEs emission (E_{PL}) is red-shifted at low temperature.[28] The electron-phonon coupling is strongly related to the FWHM of the emission band, and it can be described by the equation[22]:

$$FWHM(T) = 2.36\sqrt{S}\hbar\omega_{phonon}\sqrt{\coth\frac{\hbar\omega_{phonon}}{2K_BT}} \tag{3}$$

Where $\hbar\omega_{phonon}$, k_B and T refer to the phonon frequency, Boltzmann constant and temperature, respectively. Then Huang-Rhys electron-phonon coupling parameter S can be calculated by fitting the temperature dependent FWHM of the emission with the above equation. For $Cs_2AgBiCl_6$, the value derived from the Huang-Rhys coupling S is extremely high (Figure S10),

WILEY-VCH

and such a strong electron-phonon coupling is also reasonable, because the high *S* value of 120

and 188 had been reported in LiI and $Cs_2NaInCl_6$, respectively.[12d, 29] A larger *S* corresponds to

a stronger tendency to form the STEs and leads to a larger coordinate difference (ΔQ) between

free exciton state and STEs. Excessively large *S* leads to the excited and ground state curves to

cross in the configuration coordinate diagram, which means that some excited state electrons

and holes can recombine nonradiative through thermally activated cross-over resulting in

reduced emission intensity. In addition, we also used Fröhlich longitudinal optical phonon

broadening model to better understand the interactions between electrons and phonons[29]:

$$\Gamma(T) = \ \Gamma_0 + \Gamma_{ac} + \Gamma_{LO} + \Gamma_{imp} = \ \Gamma_0 + \gamma_{ac}T \ + \gamma_{LO}\left(e^{-\frac{E_{LO}}{K_BT}} - 1\right)^{-1} + \gamma_{imp}e^{-\frac{E_{imp}}{K_BT}} \tag{4}$$

Here Γ_0 is a temperature independent term which arises from scattering due to disorder and

imperfections, Γ_{ac} and Γ_{LO} represent the acoustic and longitudinal optical phonon (Fröhlich)

interactions, Γ_{LO} was the phonon energy and the final term Γ_{imp} describes the contribution of

ionized impurities. Both Γ_{ac} and Γ_{imp} can be ignored, so the main contribution to the FWHM

is the Γ_{LO}. The terms Γ_0 and Γ_{LO} produce an excellent fit with Γ_0=456.1 meV, γ_{LO}=226.3

meV for $Cs_2AgBiCl_6$, and Γ_0=473.8 meV, γ_{LO} =75.6 meV for $Cs_2Ag_{0.05}Na_{0.95}BiCl_6$,

respectively. The high value of the Fröhlich coupling constant γ_{LO} (226.3 meV) of

$Cs_2AgBiCl_6$ in comparison to that of the 3D hybrid perovskites (40-61 meV) suggest the greater

strength of the electron-phonon coupling in $Cs_2AgBiCl_6$[30], which will causes the energy of the

excited state to be dissipated by the phonons. Similar to the Huang-Kun factor, a significant

decrease coupling strength was observed in $Cs_2Ag_{0.05}Na_{0.95}BiCl_6$ (75.6 meV), resulting in a less

pronounced temperature broadening of the emission spectrum after the introduction of Na ions.

This prevents the temperature quenching of the emission caused by strong electron-phonon

coupling (Figure 5d). The Raman spectra shown in Figure 5e also proves that the introduction

of Na ions can reduce the electron-phonon interaction, resulting in a weakening of non-radiative

transitions and an enhanced effect of PLQY.[31] A schematic diagram of the model before and

10

after the introduction of Na ions is presented in the Figure 5f to illustrate the luminescence mechanism and to explain the difference in thermal quenching behavior. The delocalized hole wave functions, low exciton binding energy and the excessive electron-phonon coupling are the reasons for the poor PLQY of $Cs_2AgBiCl_6$ at room temperature. The main role of Na ions is to act as a barrier to break the connections between $[AgCl_6]^{5-}$ octahedrons and thus causes the localization of the electron-hole wave function centered on Ag ions and the formation of localized STEs. As a result, the exciton binding energy increases with the introduction of Na ions and contributes to reduced thermal quenching of the exciton emission at room temperature, corresponding to more excitons in the self-trapped state in the Figure 5f. Besides, a high fraction of Na ions significantly weakens the strong electron-phonon coupling in the original system, reduces the ΔQ and prevents the thermally activated cross-over of the excited state and ground state curves in the coordinate diagram, achieving efficient emission at room temperature.

Apart from the excellent optical properties, stability is also a key factor that must be considered in the application of materials. Due to the all-inorganic composition, the $Cs_2Ag_{0.05}Na_{0.95}BiCl_6$ maintains structural integrity when the temperature is up to 550 ℃ (Figure S11a). It also showed a good humidity stability with little change in PXRD pattern after six months of storage in an ambient atmosphere of 40% humidity (Figure S11b). In addition, the PLQY was also detected at one month and six months after synthesis. The results showed that the quantum efficiency of the sample remained at 90% of the initial value after six months in air (Figure S11c). The excellent stability and the outstanding optical performance make $Cs_2Ag_{0.05}Na_{0.95}BiCl_6$ be a promising NIR light emitter for optoelectronic applications, which will be discussed in the following.

The $Cs_2Ag_{0.05}Na_{0.95}BiCl_6$ single crystal has an ultra-broad emission covering the NIR region, high PLQY and stability, offering its potential application for NIR spectral detection and night vision. To test the performance, a NIR LED was fabricated by combining a commercial near-ultraviolet (365 nm) LED chip with $Cs_2Ag_{0.05}Na_{0.95}BiCl_6$ single crystal shown

11

in Figure 6a. To demonstrate the light penetration in tissue, three different parts of meat tissues were obtained from the same piece of meat and cut into same thicknesses (about 2 mm thick) as shown in the inset Figure 6b. The spectrum of the LED device and the spectrum of the device after penetration through various tissues are shown in the Figure 6b. The emission of the UV chip could not penetrate the three kinds of tissues. After penetrating the tissue, only the spectrum of the red/NIR area was detected. Compared to the initial emission intensity, the remaining intensities after penetrating lean, skin and fat are 48.8%, 27.5% and 21.6%, respectively. In addition, after penetrating three kinds of tissues together, the remaining intensity can reach more than 5% and proves the sufficient penetration depth. This demonstrates that we can evaluate the composition of biological tissue according to the ratio of remaining intensity to initial intensity after penetration (Figure S12a-d, Supporting Information). The photographs taken with different cameras under natural light and NIR LED are shown to exhibit the application of the fabricated NIR LED in night vision. It can be observed that when the NIR LED device is turned off, the NIR camera cannot capture any image (Figure 6d). When the NIR LED is turned on, the NIR camera can clearly capture the outline of the flower and the shadow under the NIR LED light, and display it in black and white colors (Figure 6e). These results show the potential application of $Cs_2Ag_{0.05}Na_{0.95}BiCl_6$ single crystal in night vision.

Conclusion

In summary, we prepared $Cs_2(Ag,Na)BiCl_6$ single crystals with a double perovskite structure and analyzed PL performance, which was improved by introducing Na ions. It is found that the reason for the weak emission of $Cs_2AgBiCl_6$ single crystal is the nonradiative transition caused by the excessive electron-phonon coupling. The introduction of Na ions into $Cs_2AgBiCl_6$ can greatly enhances its emission quantum efficiency (~1%), and the $Cs_2Ag_{0.05}Na_{0.95}BiCl_6$ has a quantum efficiency of 51%. Temperature dependent-optical properties studies demonstrate the emission originates from the self-trapped state. The DFT calculations show that the main contribution of Na ions in the energy band structure is to

12

WILEY-VCH

weaken coupling between $[AgCl_6]^{5-}$ octahedrons and to realize localized electron and hole wave functions, which promotes the formation of STEs. The introduction of Na ions weakens the strong coupling between electrons and phonons. This is evident from less thermal broadening, a smaller Fröhlich coupling constant and a higher luminescence quenching temperature which explains the efficient broadband emission at room temperature for $Cs_2Ag_{0.05}Na_{0.95}BiCl_6$. The $Cs_2Ag_{0.05}Na_{0.95}BiCl_6$ single crystal shows good stability to heat and long term exposure to ambient air. The high efficiency, broad NIR emission and high stability make $Cs_2Ag_{0.05}Na_{0.95}BiCl_6$ promising for application as emitter in phosphor converted NIR LEDs. The potential application of the $Cs_2Ag_{0.05}Na_{0.95}BiCl_6$ was successfully demonsrated by constrcuring a NIR LED,which was then used to evaluate the the composition of biological tissue and night vision.

Supporting Information

Experimental Section, ICP-OES data, Single crystal X-ray diffraction data, PXRD spectra, High-resolution XPS spectra, Decay time, the quantum efficiency, PLE and PL spectra, Power-dependent PL spectra, TRPL mapping, The band structures of $Cs_2AgBiCl_6$ and $Cs_2NaBiCl_6$, Temperature-dependent PL spectra, Temperature-dependent FWHM, TGA thermogram of $Cs_2Ag_{0.05}Na_{0.95}BiCl_6$, NIR-LED transmission images.

Acknowledgements

13

WILEY-VCH

Conflict of Interest
There is no conflict of interest to declare.

References

$Cs_2Ag_{0.05}Na_{0.95}BiCl_6$: Deposition Number 2177254

[1]   a) N. Tessler, V. Medvedev, M. Kazes, S. Kan, U. Banin, *Science* **2002**, *295*, 1506-1508; b) E. J. Marques, S. T. de Freitas, M. F. Pimentel, C. Pasquini, *Food Chem.* **2016**, *197 Pt B*, 1207-1214; c) D. Hayashi, A. M. van Dongen, J. Boerekamp, S. Spoor, G. Lucassen, J. Schleipen, *Appl. Phys. Lett.* **2017**, *110*, 233701; d) Y. Fan, P. Wang, Y. Lu, R. Wang, L. Zhou, X. Zheng, X. Li, J. A. Piper, F. Zhang, *Nat. Nanotechnol.* **2018**, *13*, 941-946; e) C. Dincer, R. Bruch, E. Costa-Rama, M. T. Fernandez-Abedul, A. Merkoci, A. Manz, G. A. Urban, F. Guder, *Adv. Mater.* **2019**, *31*, 1806739; f) A. Zampetti, A. Minotto, F. Cacialli, *Adv. Funct. Mater.* **2019**, *29*, 1807623; g) X. Zhao, Z.-K. Tan, *Nat. Photonics* **2019**, *14*, 215-218.

[2]   a) M.-H. Fang, P.-Y. Huang, Z. Bao, N. Majewska, T. Leśniewski, S. Mahlik, M. Grinberg, G. Leniec, S. M. Kaczmarek, C.-W. Yang, K.-M. Lu, H.-S. Sheu, R.-S. Liu, *Chem. Mater.* **2020**, *32*, 2166-2171; b) A. Minotto, I. Bulut, A. G. Rapidis, G. Carnicella, M. Patrini, E. Lunedei, H. L. Anderson, F. Cacialli, *Light Sci. Appl.* **2021**, *10*, 18.

[3]   C. T. Jackson, S. Jeong, G. F. Dorlhiac, M. P. Landry, *iScience* **2021**, *24*, 102156.

[4]   a) D. Rajesh, R. J. Amjad, M. Reza Dousti, A. S. S. de Camargo, *J. Alloys Compd.* **2017**, *695*, 607-612; b) R. A. Talewar, Sk. Mahamuda, A. S. Rao, C. P. Joshi, S. V. Moharil, *J. Lumin.* **2018**, *202*, 1; c) S. Nishimura, S. Fuchi, Y. Takeda, *J. Mater. Sci. Mater. Electron.* **2017**, *28*, 7157-7162; d) S. Fuchi, Y. Takeda, *Physica Status Solidi(c)* **2011**, *8*, 2653-2656.

[5]   a) Z. Tang, F. Du, H. Liu, Z. Leng, X. Sun, H. Xie, M. Que, Y. Wang, Adv. Opt. Mater. **2022**, 2102204; b) J. Qiao, G. Zhou, Y. Zhou, Q. Zhang, Z. Xia, *Nat. Commun.* **2019**, *10*, 5267.

[6]   a) Z. Li, Y. Zhang, X. Wu, X. Wu, R. Maudgal, H. Zhang, G. Han, *Adv. Sci.* **2015**, *2*, 1500001; b) E. Song, H. Ming, Y. Zhou, F. He, J. Wu, Z. Xia, Q. Zhang, *Laser Photonics Rev.* **2020**, *15*, 2000410.

[7]   a) D. Huang, S. Liang, D. Chen, J. Hu, K. Xu, H. Zhu, *Chem. Eng. J.* **2021**, *426*, 131332; b) Z. Jia, C. Yuan, Y. Liu, X. J. Wang, P. Sun, L. Wang, H. Jiang, J. Jiang, *Light Sci. Appl.* **2020**, *9*, 86; c) C. Yuan, R. Li, Y. Liu, L. Zhang, J. Zhang, G. Leniec, P. Sun, Z. Liu, Z. Luo, R. Dong, J. Jiang, *Laser Photonics Rev.* **2021**, *15*, 2100227.

[8]   Y. Jiang, J. Li, X. Zhen, C. Xie, K. Pu, *Adv. Mater.* **2018**, *30*, 1705980.

[9]   S. He, L. Zhang, H. Wu, H. Wu, G. Pan, Z. Hao, X. Zhang, L. Zhang, H. Zhang, J. Zhang, *Adv. Opt. Mater.* **2020**, *8*, 1901684.

[10]   L. Wang, P. Li, R. Duan, X. He, *Expos. Health* **2021**, 239-251.

[11]   a) M. D. Smith, H. I. Karunadasa, *Acc. Chem. Res.* **2018**, *51*, 619-627; b) S. Yakunin,

B. M. Benin, Y. Shynkarenko, O. Nazarenko, M. I. Bodnarchuk, D. N. Dirin, C. Hofer, S. Cattaneo, M. V. Kovalenko, *Nat. Mater.* **2019**, *18*, 846-852; c) X. Mo, T. Li, F. Huang, Z. Li, Y. Zhou, T. Lin, Y. Ouyang, X. Tao, C. Pan, *Nano Energy* **2021**, *81*, 105570.

[12]   a) M. Li, Z. Xia, *Chem. Soc. Rev.* **2021**, *50*, 2626-2662; b) P. Cheng, L. Feng, Y. Liu, D. Zheng, Y. Sang, W. Zhao, Y. Yang, S. Yang, D. Wei, G. Wang, K. Han, *Angew. Chem. Int. Ed.* **2020**, *59*, 21414-21418; c) C.-Y. Wang, P. Liang, R.-J. Xie, Y. Yao, P. Liu, Y. Yang, J. Hu, L. Shao, X. W. Sun, F. Kang, G. Wei, *Chem. Mater.* **2020**, *32*, 7814-7821; d) J. Luo, X. Wang, S. Li, J. Liu, Y. Guo, G. Niu, L. Yao, Y. Fu, L. Gao, Q. Dong, C. Zhao, M. Leng, F. Ma, W. Liang, L. Wang, S. Jin, J. Han, L. Zhang, J. Etheridge, J. Wang, Y. Yan, E. H. Sargent, J. Tang, *Nature* **2018**, *563*, 541-545.

[13]   M. L. Lai, T. Y. Tay, A. Sadhanala, S. E. Dutton, G. Li, R. H. Friend, Z. K. Tan, *J. Phys. Chem. Lett.* **2016**, *7*, 2653-2658.

[14]   a) J. Yu, J. Kong, W. Hao, X. Guo, H. He, W. R. Leow, Z. Liu, P. Cai, G. Qian, S. Li, X. Chen, X. Chen, *Adv. Mater.* **2019**, *31*, 1806385; b) X. Wang, Q. Shen, Y. Chen, N. Ali, Z. Ren, G. Bi, H. Wu, *Nanoscale* **2021**, *13*, 15285-15291.

[15]   a) A. Noculak, V. Morad, K. M. McCall, S. Yakunin, Y. Shynkarenko, M. Worle, M. V. Kovalenko, *Chem. Mater.* **2020**, *32*, 5118-5124; b) B. Chen, Y. Guo, Y. Wang, Z. Liu, Q. Wei, S. Wang, A. L. Rogach, G. Xing, P. Shi, F. Wang, *J. Am. Chem. Soc.* **2021**, *143*, 17599-17606; c) V. Morad, S. Yakunin, M. V. Kovalenko, *ACS Mater. Lett.* **2020**, *2*, 845-852; d) R. Zeng, L. Zhang, Y. Xue, B. Ke, Z. Zhao, D. Huang, Q. Wei, W. Zhou, B. Zou, *J. Phys. Chem. Lett.* **2020**, *11*, 2053-2061; e) L. Zhou, J. F. Liao, Y. Qin, X. D. Wang, J. H. Wei, M. Li, D. B. Kuang, R. He, *Adv. Funct. Mater.* **2021**, *31*, 2102654.

[16]   a) W. Zheng, R. Sun, Y. Liu, X. Wang, N. Liu, Y. Ji, L. Wang, H. Liu, Y. Zhang, *ACS Appl. Mater. Inter.* **2021**, *13*, 6404-6410; b) B. Zhou, Z. Liu, S. Fang, H. Zhong, B. Tian, Y. Wang, H. Li, H. Hu, Y. Shi, *ACS Energy Lett.* **2021**, *6*, 3343-3351.

[17]   X. Cheng, R. Li, W. Zheng, D. Tu, X. Shang, Z. Gong, J. Xu, S. Han, X. Chen, *Adv. Opt. Mater.* **2021**, *9*, 2100434.

[18]   B. Su, M. Li, E. Song, Z. Xia, *Adv. Funct. Mater.* **2021**, *31*, 2105316.

[19]   T. W. Lim, S. D. Kim, K. D. Sung, Y. M. Rhyim, H. Jeen, J. Yun, K. H. Kim, K. M. Song, S. Lee, S. Y. Chung, M. Choi, S. Y. Choi, *Sci. Rep.* **2016**, *6*, 19746.

[20]   R. S. Lamba, P. Basera, S. Bhattacharya, S. Sapra, *J. Phys. Chem. Lett.* **2019**, *10*, 5173-5181.

[21]   E. R. Dohner, A. Jaffe, L. R. Bradshaw, H. I. Karunadasa, *J. Am. Chem. Soc.* **2014**, *136*, 13154-13157.

[22]   S. Li, J. Luo, J. Liu, J. Tang, *J. Phys. Chem. Lett.* **2019**, *10*, 1999-2007.

[23]   C.-M. Dai, T. Zhang, Y. N. Wu, S. Chen, *Adv. Funct. Mater.* **2020**, *30*, 2000653.

[24]   Z. W. Xiao, W. W. Meng, J. B. Wang, D. B. Mitzi, Y. F. Yan, *Materials Horizons* **2017**, *4*, 206-216.

[25]   D. Zhu, J. Zito, V. Pinchetti, Z. Dang, A. Olivati, L. Pasquale, A. Tang, M. L. Zaffalon, F. Meinardi, I. Infante, L. De Trizio, L. Manna, S. Brovelli, *ACS Energy Lett.* **2020**, *5*, 1840-1847.

[26]   a) Y. Zhang, X. Liu, H. Sun, J. Zhang, X. Gao, C. Yang, Q. Li, H. Jiang, J. Wang, D. Xu, *Angew. Chem. Int. Ed.* **2021**, *60*, 7587-7592; b) L. Gan, J. Li, Z. Fang, H. He, Z. Ye, *J. Phys. Chem. Lett.* **2017**, *8*, 5177-5183.

[27]   B. Ke, R. Zeng, Z. Zhao, Q. Wei, X. Xue, K. Bai, C. Cai, W. Zhou, Z. Xia, B. Zou, *J. Phys. Chem. Lett.* **2020**, *11*, 340-348.

[28]   K. Dawson, D. Pooley, *Physica Status Solidi(b)* **1969**, *35*, 95-105.

[29]   S. Rudin, T. L. Reinecke and B. Segall, *Phys. Rev. B* **1990**, 42, 11218.

[30]   A. D. Wright, C. Verdi, R. L. Milot, G. E. Eperon, M. A. Perez-Osorio, H. J. Snaith, F. Giustino, M. B. Johnston, L. M. Herz, *Nat. Commun.* **2016**, 7, 11755.

[31]   a) L. Zhang, Y. Fang, L. Sui, J. Yan, K. Wang, K. Yuan, W. L. Mao, B. Zou, *ACS Energy*

WILEY-VCH

Lett. **2019**, *4*, 2975-2982; b) L. Zhou, J. F. Liao, Z. G. Huang, J. H. Wei, X. D. Wang, H. Y. Chen, D. B. Kuang, *Angew. Chem. Int. Ed.* **2019**, *43*, 15581-15586.
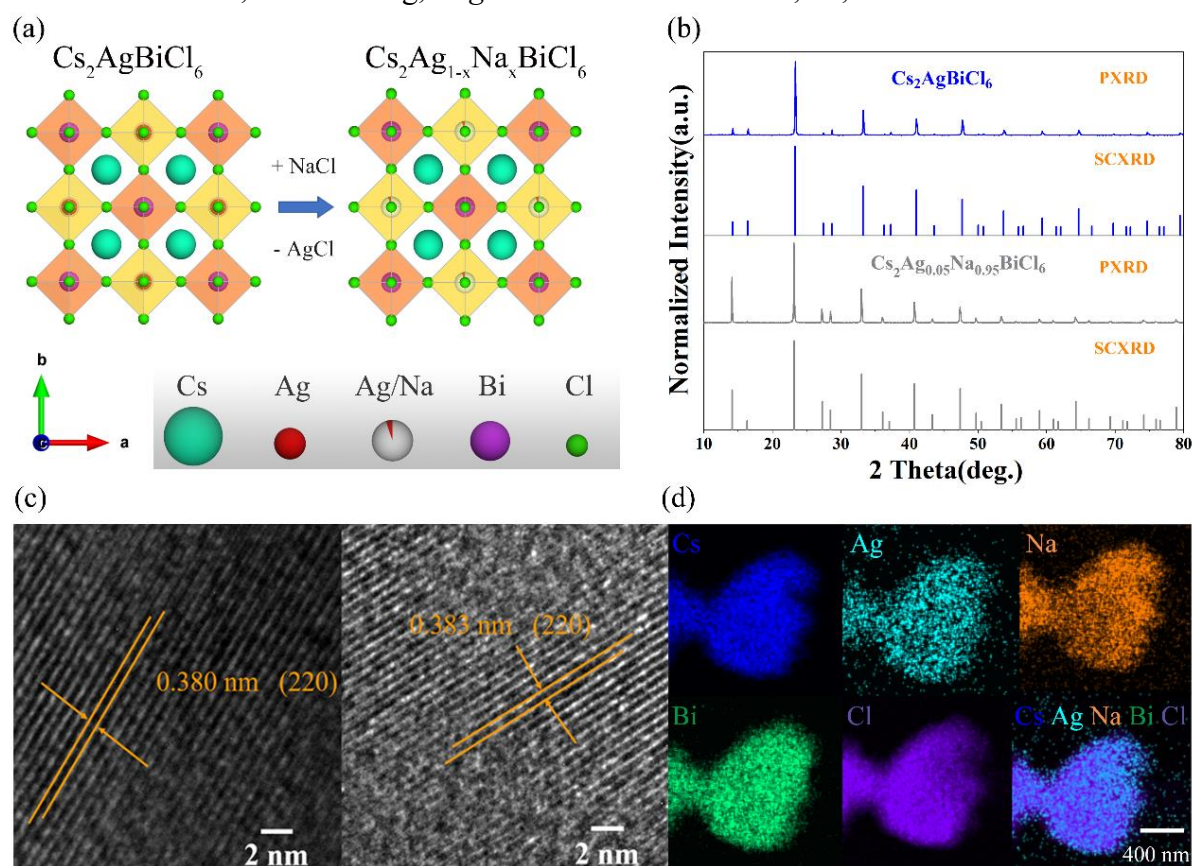
Figure 1. (a) Crystal structure of $Cs_2AgBiCl_6$ and $Cs_2Ag_{1-x}Na_xBiCl_6$. (b) Power XRD and Single Crystal XRD patterns of $Cs_2AgBiCl_6$ and $Cs_2Ag_{0.05}Na_{0.95}BiCl_6$. (c) HRTEM images of $Cs_2AgBiCl_6$ (left) and $Cs_2Ag_{0.05}Na_{0.95}BiCl_6$ (right). (d) EDS elemental mapping image of $Cs_2Ag_{0.05}Na_{0.95}BiCl_6$.

WILEY-VCH
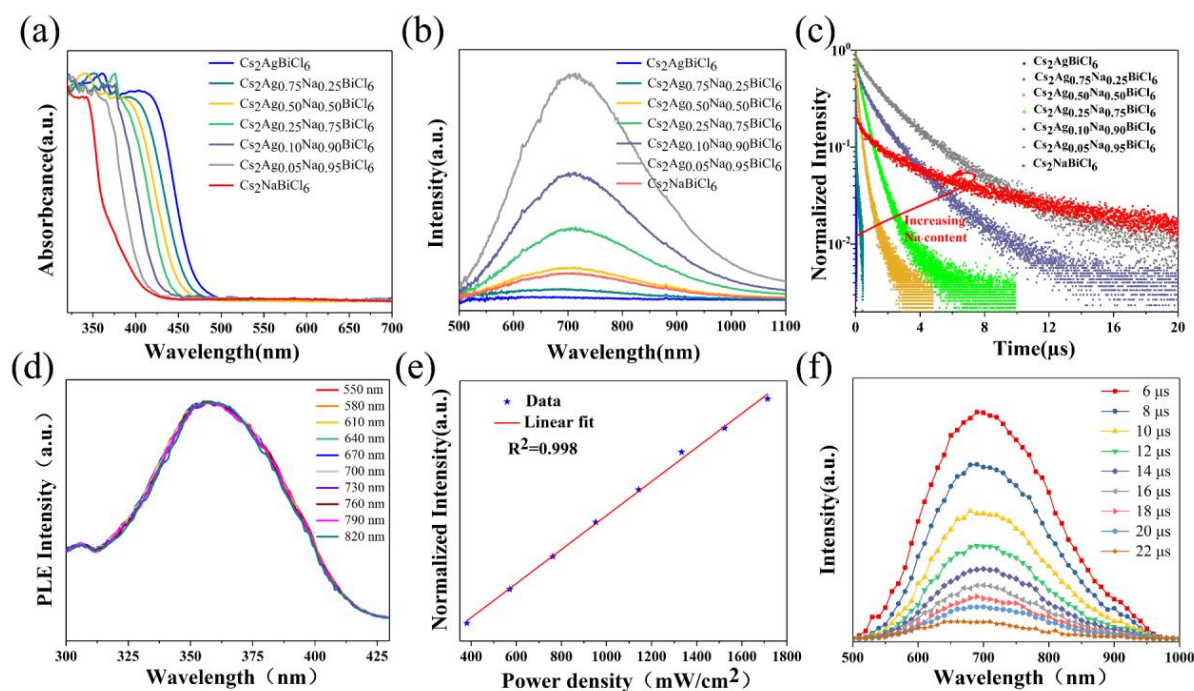
Figure 2. (a) UV-vis absorption of spectra of $Cs_2Ag_{1-x}Na_xBiCl_6$. (b) Photoluminescence spectra of $Cs_2Ag_{1-x}Na_xBiCl_6$. (c) Photoluminescence decay curves of $Cs_2Ag_{1-x}Na_xBiCl_6$. (d) Excitation spectra of $Cs_2Ag_{0.05}Na_{0.95}BiCl_6$. (e) Integrated PL intensity of $Cs_2Ag_{0.05}Na_{0.95}BiCl_6$ as a function of excitation power density. (f) Time-resolved photoluminescence spectra of $Cs_2Ag_{0.05}Na_{0.95}BiCl_6$ from 6 to 22 µs.

17
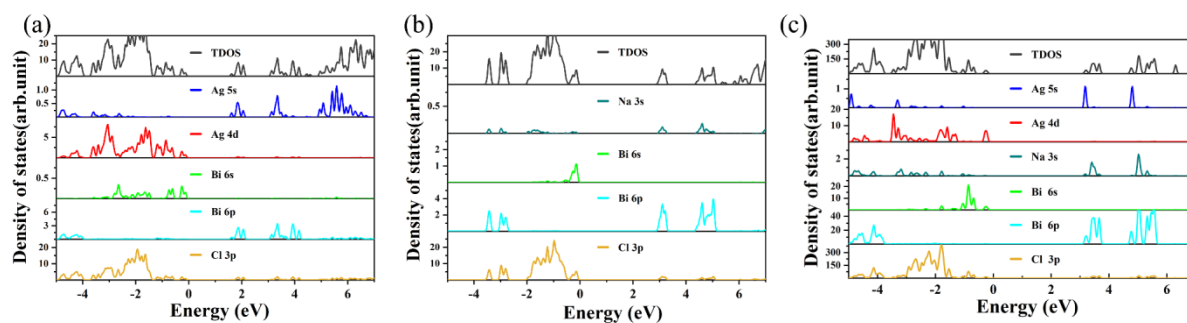
WILEY-VCH

Figure 3. The total and partial density of states of (a) $Cs_2AgBiCl_6$ and (b) $Cs_2NaBiCl_6$ from the PBE+SOC calculations. (c)The total and partial density of states of $Cs_2Ag_{0.06}Na_{0.94}BiCl_6$ from the HSE06+SOC calculations.
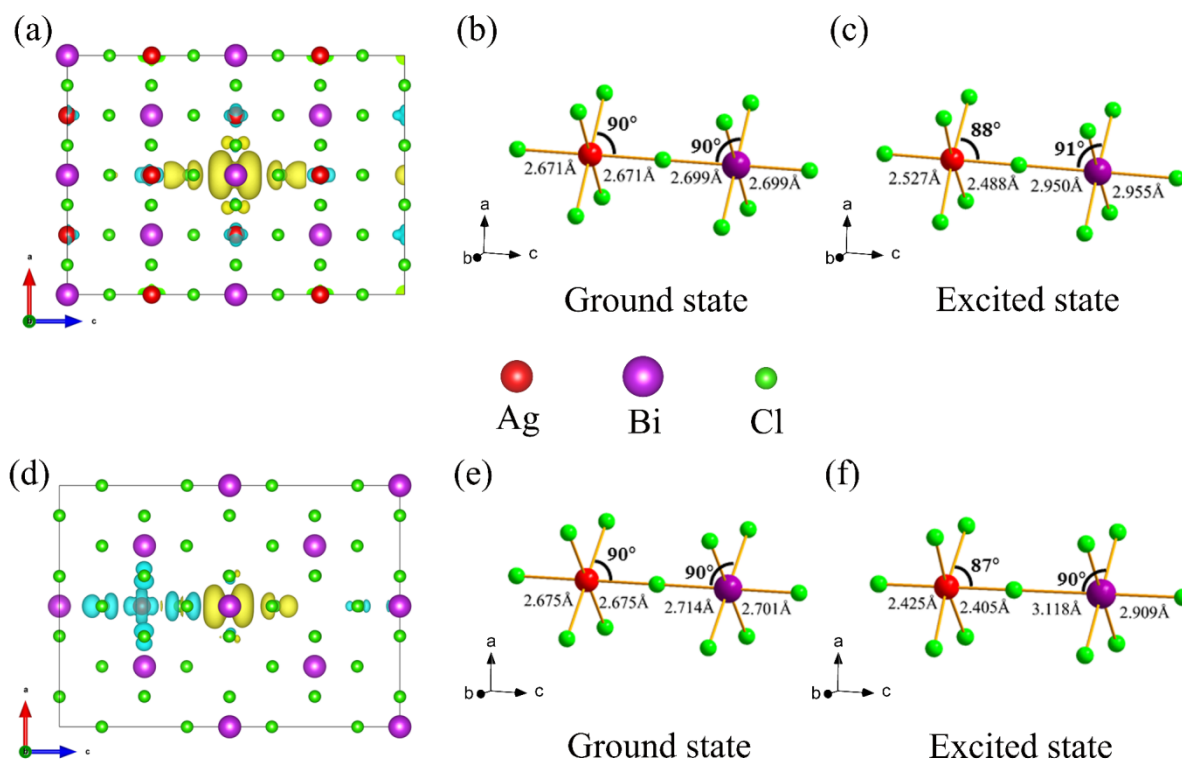
Accepted Manuscript

18

Figure 4. (a) STE in $Cs_2AgBiCl_6$. (b) equilibrium geometry structures of the ground state and (c) the excited state (STE) of $Cs_2AgBiCl_6$. (d) STE in $Cs_2Ag_{0.06}Na_{0.94}BiCl_6$. (e) equilibrium geometry structures of the ground state and (f) excited state of $Cs_2Ag_{0.06}Na_{0.94}BiCl_6$. The yellow and cyan isosurfaces denote electrons and holes, respectively.
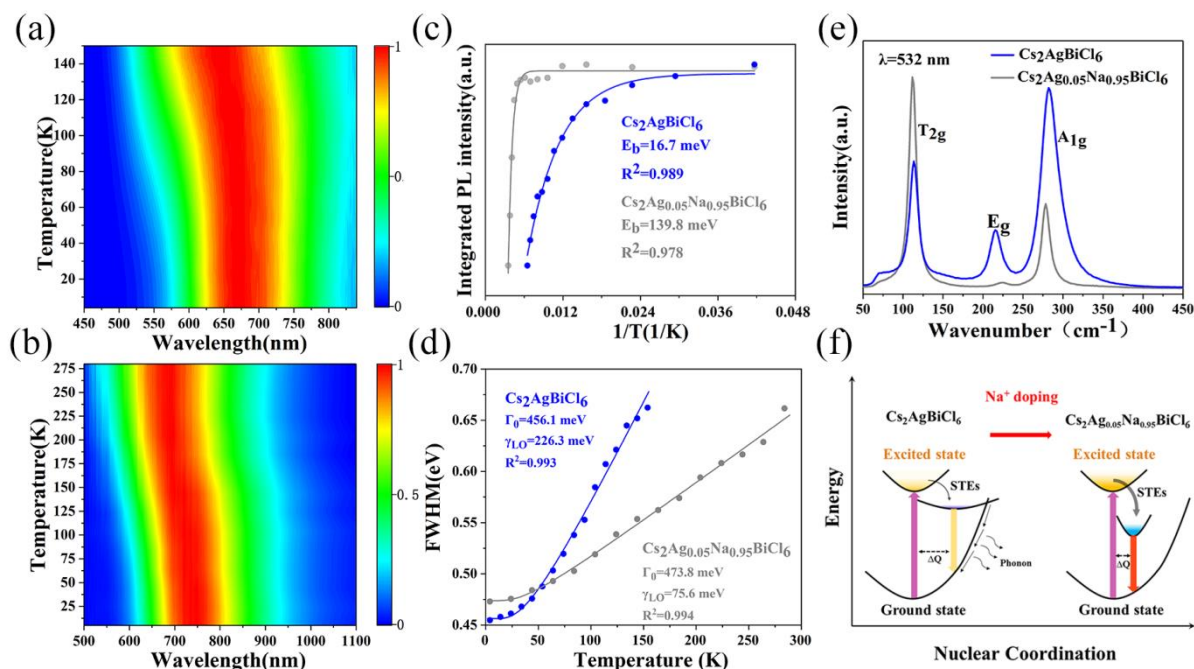
Figure 5. Color plots of the normalized PL spectra of (a) $Cs_2AgBiCl_6$ and (b) $Cs_2Ag_{0.05}Na_{0.95}BiCl_6$ at different temperatures. (c) Integrated PL intensity as a function of temperature for $Cs_2AgBiCl_6$ and $Cs_2Ag_{0.05}Na_{0.95}BiCl_6$. (d) The FWHM as a function of temperature for $Cs_2AgBiCl_6$ and $Cs_2Ag_{0.05}Na_{0.95}BiCl_6$. (e) Raman spectra for $Cs_2AgBiCl_6$ and $Cs_2Ag_{0.05}Na_{0.95}BiCl_6$ at room temperature using a 532 nm excitation laser. (f) Schematic of the photophysical processes in $Cs_2AgBiCl_6$ and $Cs_2Ag_{0.05}Na_{0.95}BiCl_6$.
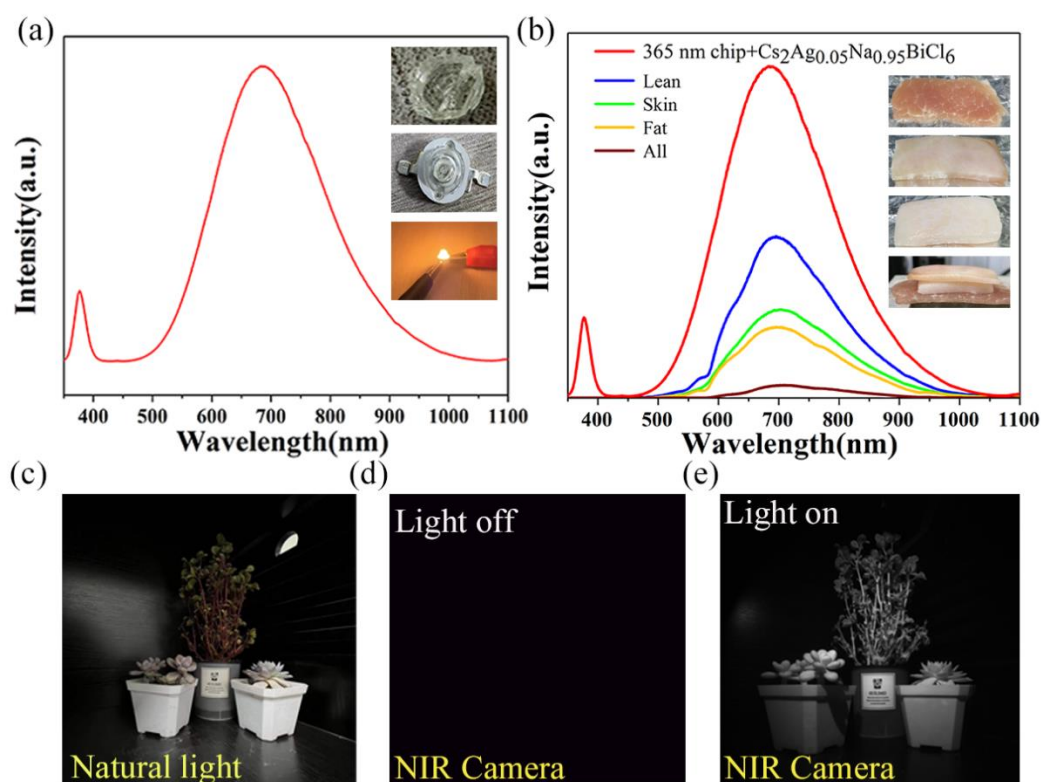
20

WILEY-VCH

Figure 6. (a) Emission spectrum of the NIR LED, Inserts show the images of $Cs_2Ag_{0.05}Na_{0.95}BiCl_6$ single crystal, NIR LED in non-powered state and powered state. (b) Initial emission of NIR LED and emission after penetrating different tissues. Inserts show the images of lean, skin, fat tissues and the three types combined. (c) Images captured by visible camera under natural light and images captured by NIR camera under NIR LED light when it is (d) off and (e) on.